

Kinetic Methods for Solving the Internal Structure of Shock Waves

Eswar Josyula,*

Air Force Research Laboratory

Kun Xu[†]

Hong Kong University of Science and Technology

Casimir J. Suchyta, III[‡]

Ohio Aerospace Institute

William F. Bailey[§]

Air Force Institute of Technology

The objective of the study is to assess the accuracy of kinetic schemes in resolving the internal structure of the shock waves. Two kinetic schemes were used, a gas kinetic BGK scheme and the direct integration of the Boltzmann equation. The argon hard sphere collision model was considered for freestream Mach numbers ranging from 1.2 to 10. The results from the calculations of the direct integration of Boltzmann equations of Ohwada were used as benchmark for Mach 1.2, 2, and 3 shock waves. The results from the direct integration solvers matched reasonably well. Agreement from gas kinetic BGK scheme at the low Mach number was good, but at higher Mach number the starting jump location was missed. A study of the velocity grid requirements for a numerical solution of the Boltzmann equation was conducted by the method developed by Tcheremissine.¹ The requirements are modest but are most stringent at the shock front location. Both the solution of the kinetic equation and the numerical evaluation of the macroscopic parameters determine the grid requirement.

Nomenclature

c	peculiar velocity
E	total energy per unit mass
f	velocity distribution function
g	anisotropic distribution function
\bar{g}	single temperature Maxwellian
k	Boltzmann constant
Kn	Knudsen number
M	Mach number
N_0	equidistant velocity nodes
N	particle number density
p	macroscopic pressure
P_{11}	xx-component of viscous stress
\mathbf{q}	heat flux vector
Q_1	streamwise component of heat flux
R	gas constant
T	macroscopic temperature
u, v, w	macroscopic velocities in x, y, z directions
v_0	velocity bin size
V	volume in velocity space
ξ_1, ξ_2, ξ_3	components of particle velocity
\mathbf{u}	velocity vector
λ	mean free path
γ	ratio of specific heats, velocity node

*Senior Research Aerospace Engineer, Air Vehicles Directorate, AFRL/RBAC, Wright-Patterson AFB, Ohio, AIAA Associate Fellow.

[†]Professor, Department of Mathematics, Hong Kong University of Science and Technology, Kowloon, Hong Kong, AIAA Member.

[‡]Senior Researcher, Ohio Aerospace Institute, AFRL/RBAC, Wright-Patterson AFB, Ohio

[§]Associate Professor, Department of Physics, AFIT/ENP, Wright-Patterson AFB, Ohio

μ	dynamical viscosity
τ	particle collision time
ρ	mass density

A. Subscripts

u	(shock) upstream conditions
d	(shock) downstream conditions
γ	at velocity node

Introduction

The kinetic description of nonequilibrium for high speed flows in upper atmosphere involves treatment of translational nonequilibrium coupled to internal degrees of excitation of the gas. In the rarefied regime, the DSMC is often used in the prediction of the aerodynamic quantities. In the transition to rarefied regime, the high cost of DSMC has led investigators to develop gas kinetic schemes, in which thermal equilibrium is assumed to be established relatively fast for the translational degree of freedom compared to internal degrees of freedom. Exchange of momentum and kinetic energy among particles can result in establishing the equilibrium Maxwellian distribution. The relaxation time for establishing a Maxwellian distribution in components of air is of the order of the average time between gas kinetic collisions.

$$\tau_{trans} \approx \tau_{gas} = \frac{\lambda}{v} = \frac{1}{Nv\sigma_{gas}} \quad (1)$$

Here λ is the gas kinetic mean free path, v is the average particle velocity, N is the particle number density, and σ_{gas} is the gas kinetic collision cross section. In air at standard conditions, $\lambda \approx 6 \times 10^{-6}$ cm and $\tau_{trans} \approx 10^{-10}$ sec. Usually the gas kinetic times are small in comparison with the flow times over which appreciable changes in the macroscopic parameters of the gas, density or energy, take place. When these conditions are satisfied it is possible to assign at every instant of time a “translational” temperature, which characterizes the average kinetic energy of translational motion of the particles. However, when the velocity distribution function of the particles is anisotropic, as is the case in low density, hypersonic nonequilibrium flows, multiple translational temperatures, one in the direction of flow and the other in the direction perpendicular to the flow, need to be delineated.

The last decade has seen a resurgence of direct methods in the numerical solution of the Boltzmann equation, the integro-differential equation describing the rate of change of the distribution function with respect to position and time.²⁻⁵ A gas kinetic, multi-temperature model for a monatomic gas was developed using equations derived from the Boltzmann equation with a first order Chapman-Enskog expansion of an anisotropic velocity distribution function.^{6,7} The model, extended to rotational nonequilibrium, was employed for computing highly nonequilibrium shock structures and compared with DSMC solutions and experimental data. The equations with generalization of the dissipative coefficients based on the closed form solution of the Bhatnagar-Gross-Krook (BGK) model of the Boltzmann equation were solved using the gas kinetic numerical scheme. Calculations of shock structure were presented for monatomic and diatomic gases in the Mach number range of 1.2 to 12.9.^{8,9} Gas kinetic schemes are computationally very efficient compared to direct Boltzmann equation methods and DSMC in the transition regime. However, a proper understanding of the evolution of the distribution function in aerodynamic flows of interest will allow realistic nonequilibrium models to be developed for the gas kinetic schemes. This is the objective of the present study. In the present study, the Boltzmann solver of Tcheremissine¹ was used for conducting different studies in the shock waves and the results from the work of Ohwada¹⁰ are as benchmark for comparison.

The present study simulates nonequilibrium relaxation in high speed flows to characterize the internal structure of the shock wave considering multi-translational temperatures in monatomic gas flow. The direct numerical integration of the Boltzmann equation for a monatomic gas was performed and shock structures from Mach 1.2 to 10 were simulated and compared with independent solutions for the hard sphere collision model. The effect of different velocity grids on the solution accuracy was studied for the direct integration of the Boltzmann equation. From the evolution of the distribution function, a simple analytic function was proposed for possible use in gas kinetic schemes for computing hypersonic flows. A validation study of the gas kinetic BGK scheme was performed to assess accuracy issues in hypersonic flows.

Analysis

Direct Integration of Boltzmann equation

The Boltzmann equation expresses the behavior of many-particle kinetic system in terms of the evolution equation for the single particle gas distribution function. The Boltzmann equation is written as

$$\frac{\partial f}{\partial t} + \boldsymbol{\xi} \frac{\partial f}{\partial \mathbf{x}} = I(\boldsymbol{\xi}) \quad (2)$$

where f , the distribution function, gives the number density at position \mathbf{x} and velocity $\boldsymbol{\xi}$ at time t . The left hand side of the above equation represents the free streaming of molecules in space, and the right side denotes the collision term. If the distribution function f is known, macroscopic variables of the mass, momentum, energy and stress can be obtained by integration. Equation 2 is solved on a grid \mathbf{x}_i in physical space and on a uniform grid consisting of N_0 equidistant velocity nodes ξ_γ with a mesh size h introduced in a domain Ω of volume V .

In the basis of three-dimensional delta functions, the distribution function and the collision integral can be represented in the form¹

$$f(\boldsymbol{\xi}, x, t) = \sum_{\gamma=1}^{N_0} f_\gamma(x, t) \delta(\boldsymbol{\xi} - \boldsymbol{\xi}_\gamma), \quad I(\boldsymbol{\xi}, x, t) = \sum_{\gamma=1}^{N_0} I_\gamma(x, t) \delta(\boldsymbol{\xi} - \boldsymbol{\xi}_\gamma) \quad (3)$$

After determining the expansion coefficients for the collision integral in the Eqns 3, the problem is reduced to solving the system of equations

$$\frac{\partial f_\gamma}{\partial t} + \boldsymbol{\xi}_\gamma \frac{\partial f_\gamma}{\partial x} = I_\gamma \quad (4)$$

by the finite difference method. In the integration of expansion of Eqn. 3 for the distribution function with weights $\Psi = (m, m\boldsymbol{\xi}, m\xi^2/2)$, the macroscopic quantities, the density ρ , the velocity \mathbf{u} , the pressure tensor \mathbf{P} and the heat flux vector \mathbf{q} are determined as the sums:

$$\rho = mv_0 \sum_{\gamma} f_\gamma, \quad \mathbf{u} = \frac{mv_0}{\rho} \sum_{\gamma} f_\gamma \boldsymbol{\xi}_\gamma, \quad P_{ij} = mv_0 \sum_{\gamma} f_\gamma c_{i,\gamma} c_{j,\gamma}, \quad q_i = \frac{mv_0}{2} \sum_{\gamma} f_\gamma c_{i,\gamma} c_\gamma^2 \quad (5)$$

where $v_0 = \frac{V}{N_0}$, $\mathbf{c}_\gamma = \boldsymbol{\xi}_\gamma - \mathbf{u}$, and $c_\gamma^2 = c_{1,\gamma}^2 + c_{2,\gamma}^2 + c_{3,\gamma}^2$

The evaluation of the collision integral is according to the conservative projection method proposed by Tcheremissine.¹

Gas Kinetic BGK Scheme

The Boltzmann equation with the simplified collision model of Bhatnagar Gross Krook (BGK) is formulated as

$$\frac{\partial f}{\partial t} + \boldsymbol{\xi} \cdot \frac{\partial f}{\partial \mathbf{x}} = \frac{f^{eq} - f}{\tau} \quad (6)$$

In the BGK model, the collision operator involves a simple relaxation to a local equilibrium distribution function f^{eq} with a characteristic time scale τ . The BGK model was proposed to describe the essential physics of molecular interactions, with τ chosen as the molecular collision time. Based on the above BGK model, the Navier-Stokes equations can be obtained with the Chapman-Enskog expansion truncated to the 1st-order,

$$\begin{aligned} f &= f^{eq} + Kn f_1 \\ &= f^{eq} - \tau (\partial f^{eq} / \partial t + \boldsymbol{\xi} \cdot \partial f^{eq} / \partial \mathbf{x}). \end{aligned} \quad (7)$$

where, f^{eq} denotes the contribution of the equilibrium part and $Kn f_1$ the nonequilibrium component. With the modification of the particle collision time, the validity of the kinetic model is extended beyond that of the Navier-Stokes equations. An earlier attempt based on this model was successful for shock structure calculations of the monatomic gas with a single translational temperature.¹¹

In the following section, the modification to Eq. 6 to formulate a multiple translational temperature model is presented.

Multi-translational temperature modeling

Assuming an anisotropic distribution for a gas with different translational temperatures in the x , y , and z directions, the equations governing the one-dimensional flow assuming equilibrium in a given direction can be written as:

$$g = \rho \left(\frac{\lambda_x}{\pi}\right)^{1/2} \left(\frac{\lambda_y}{\pi}\right)^{1/2} \left(\frac{\lambda_z}{\pi}\right)^{1/2} \exp[-\lambda_x(\xi_1 - u)^2 - \lambda_y \xi_2^2 - \lambda_z \xi_3^2], \quad (8)$$

where ρ is the mass density, u is the macroscopic velocity in the x -direction, and (ξ_1, ξ_2, ξ_3) the components of the particle velocity in the x , y and z directions, respectively. The parameter λ is related to the gas temperature, given by $\lambda_x = \mathcal{M}/2kT_x$, $\lambda_y = \mathcal{M}/2kT_y$ and $\lambda_z = \mathcal{M}/2kT_z$. For the multi-translational temperature formulation of a one dimensional flow considered in the present study, we can assume that $T_y = T_z$, such that, $\lambda_y = \lambda_z$. The establishment of the above ellipsoidal Maxwellian distribution is assumed to be a consequence of particle collisions. Over a long period of time, the above state g will further approach an overall equilibrium state given by \bar{g} ,

$$\bar{g} = \rho \left(\frac{\lambda^{eq}}{\pi}\right)^{3/2} \exp[-\lambda^{eq}((\xi_1 - u)^2 + \xi_2^2 + \xi_3^2)] \quad (9)$$

If the mass, momentum and energy is conserved during the particle collision process, the relationship between an averaged equilibrium temperature T^{eq} ($\lambda^{eq} = \mathcal{M}/2kT^{eq}$) and the individual temperatures T_x, T_y , and T_z is given by,

$$T^{eq} = \frac{1}{3}(T_x + 2T_y), \quad (10)$$

where the assumption $T_y = T_z$ was invoked for the one-dimensional flow. The above process from g to \bar{g} can be described by the gas kinetic model

$$g_t + \xi_1 g_x = (\bar{g} - g)/\tau, \quad (11)$$

which is similar to the BGK model.¹² From the above kinetic equation, besides the Navier-Stokes equations for the mass, momentum and total energy, additional thermal energy equations for the particle random motion in the y and z directions are obtained. For the 1D case, the thermal energy equation becomes

$$(\rho T_y)_t + (\rho u T_y)_x = \frac{\rho R}{3\tau}(T_x - T_y), \quad (12)$$

where R is the gas constant and τ is the particle collision time. The two temperature, continuum Navier-Stokes formulation is given by Eq. 11. The solutions of the shock structure based on the gas kinetic scheme¹³ has similar behavior as the results of multi-temperature Navier-Stokes results in Ref. 14. The solutions in Ref. 14 are thinner with a non-physical, sharp jump in the calculated density profile inside the shock layer and are inconsistent with the DSMC solutions; the discrepancy more pronounced for the high Mach number cases. The model given by Eq. 11 was derived from Boltzmann equation, but the model to derive the macroscopic multiple temperature hydrodynamical model in Ref. 14 is inadequate, requiring further improvement. It is noted that most multi-temperature kinetic models in the literature are based on the same assumption of an ellipsoidal Maxwellian distribution.

In order to improve the previously mentioned kinetic model for the translational nonequilibrium and overcome the anomalous behavior of the shock wave solutions,¹⁴ we reconstructed the particle collision process. Starting from the gas distribution function f for a monatomic gas, the particle collisions drive f to g and \bar{g} , instead of from g to \bar{g} alone. During the course of particle collisions, it is difficult to distinguish the process from f to g or from f to \bar{g} . The particle collision time for translational nonequilibrium, however, can be assumed to be the same. Note, this should not be confused with the nonequilibrium internal energy distribution in a diatomic gas, where the collision time for the rotational relaxation may be much larger than the translational non-equilibrium relaxation. Therefore, for the monatomic gas we construct a generalized BGK model for the translational non-equilibrium,

$$f_t + \xi_1 f_x = \frac{1}{2} \left[\frac{g - f}{\tau} + \frac{\bar{g} - f}{\tau} \right] + Q, \quad (13)$$

where f is the real gas distribution function, and Q is the source term, which contributes s in Eqn. 14. Here g is the ellipsoidal Maxwellian with three temperatures and \bar{g} is the single temperature Maxwellian. The real gas distribution function, f will approach these two states. The ellipsoidal Maxwellian g which represents non-equilibrium distribution will eventually approach a single temperature Maxwellian distribution. Note that the particle collision time τ is related

to the local dynamical viscosity μ and pressure p , i.e., $\tau = \mu/p$. The relation between mass ρ , momentum ρu , total energy ρE , and the thermal energy ρE_{y-z} in the y and z directions are

$$W = \begin{pmatrix} \rho \\ \rho u \\ \rho E \\ \rho E_{y-z} \end{pmatrix} = \int \psi f d\xi_1 d\xi_2 d\xi_3,$$

where ψ has the components

$$\psi = (1, \xi_1, \frac{1}{2}(\xi_1^2 + \xi_2^2 + \xi_3^2), \frac{1}{2}(\xi_2^2 + \xi_3^2))^T.$$

Since mass, momentum and total energy are conserved during particle collisions, f and g satisfy the condition

$$\int \frac{1}{2}[(g - f) + (\bar{g} - f)]\psi_\alpha d\xi_1 d\xi_2 d\xi_3 = S = (0, 0, 0, s)^T, \quad \alpha = 1, 2, 3, 4. \quad (14)$$

The source term s can be still be modeled as $s = \rho R(T_x - T_y)/3\tau$.

For any kinetic model of multiple translational temperature non-equilibrium, the averaged temperature $T^{eq} = \frac{1}{3}(T_x + T_y + T_z)$. In the 1D case this averaged temperature should be the same temperature as the one-temperature gas kinetic model. If we take moments $(\xi_1 - u)^2$, ξ_2^2 and ξ_3^2 on the model given by Eq. 13, we can obtain the temperature evolution equations for individual directions. By adding them together and using the condition $3T = T_x + T_y + T_z$, a single equation for the averaged temperature T can be obtained,

$$(\rho T)_t + (\rho u T)_x = (\rho T^{eq} - \rho T)/\tau,$$

which is the same temperature evolution equation from a single temperature BGK model, i.e. $f_t + \xi_1 f_x = (\bar{g} - f)/\tau$. So, the averaged temperature from the two-temperature kinetic model, Eq. 13, is the same as that from a single temperature model. We can say that the model given by Eq. 13 is a valid extension to recover the multiple temperature non-equilibrium from the original BGK model.

In order to test the above model (Eq. 13), the numerical method developed in Ref. 13 was used to solve Eq. 13. For a finite volume method,

$$W_j^{n+1} = W_j^n + \frac{1}{\Delta x} \int_0^{\Delta t} (F_{j-1/2}(t) - F_{j+1/2}(t)) dt + S_j^n \Delta t, \quad (15)$$

where W_j^n is the cell averaged mass, momentum, total energy, and the thermal energy in y and z directions, and $F_{j+1/2}$ is the corresponding fluxes at a cell interface by solving Eq. 13. Note that Δt is the time step $\Delta t = t^{n+1} - t^n$, and S_j^n is the source term for the thermal energy. The evaluation of the fluxes is based on the distribution function f at a cell interface. For the shock structure calculation, due to the smoothness inside the shock layer, the gas distribution function at a cell interface is constructed using the Chapman-Enskog expansion and has the form

$$f = \frac{1}{2}(g + \bar{g}) - \frac{1}{2}\tau[g_t + \bar{g}_t + \xi_1(g_x + \bar{g}_x)] + \frac{1}{2}t(g_t + \bar{g}_t) \quad (16)$$

where the g_x and \bar{g}_x can be obtained from the gradients of macroscopic variables, and g_t and \bar{g}_t can be evaluated from the compatibility conditions

$$\int (g_t + \xi_1 g_x) \psi_\alpha d\xi_1 d\xi_2 d\xi_3 = 0 \quad \text{and} \quad \int (\bar{g}_t + \xi_1 \bar{g}_x) d\xi_1 d\xi_2 d\xi_3 = 0.$$

For more details, see Ref. 13. Even with the ability to recover two translational temperatures, the non-equilibrium distribution (Eq. 16) is truncated to the Navier-Stokes order and it will not be accurate in the description of rarefied flow. The anomalous density jump given by the model of Eq. 11(found in Ref. 14) does not appear in the solutions given by the present formulation. However, the shock thickness is still thinner in comparison with experimental measurements and the DSMC solutions. Theoretically, it seems that we should continue this expansion in Eq. 16 to go to Burnett and Super-Burnett orders. Unfortunately, the success from the higher order expansion is limited, and there is no evidence that the successive expansions converge. Additionally, we can replace the collision time τ in Eq.(16) with a generalized one, τ_* , and assume that there is a closed form solution of the BGK model. We can obtain a relation

between τ_* and τ . In the current study, the new collision model (Eq. 13) is used with BGK-Xu method¹¹ to establish a generalized particle collision time τ_* ,

$$\tau_* = \tau / (1 + \tau \langle D^2 g \rangle / \langle Dg \rangle) \quad (17)$$

where $D = \partial_t + \xi_1 \partial_x$ and $\langle \dots \rangle = \int (\dots) (\xi_1 - u)^2 d\xi_1 d\xi_2 d\xi_3$. Here τ depends on the macroscopic variables through the relation $\tau p = \mu_\infty (T/T_\infty)^\omega$, and the generalized τ_* will depend not only on the macroscopic variables, but also on their gradients. Therefore, the evaluation of τ_* represents a set of generalized constitutive relations for the calculation of the translational non-equilibrium flow. In order to simulate the flow with a realistic Prandtl number, a modification of the heat flux in the energy transport at a cell interface, as used in Ref. 13, is implemented in the current study.

Initial and Boundary Conditions

Table 1. Rankine-Hugoniot Conditions across shock wave for $\gamma=5/3$

Mach No Upstream (M_u)	Mach No Downstream (M_d)	p_d/p_u	ρ_d/ρ_u	T_d/T_u
1.2	0.846	1.55	1.297	1.195
2	0.607	4.75	2.286	2.081
3	0.522	11	3	3.667
5	0.475	31	3.571	8.68
10	0.454	124.75	3.883	32.12

The boundary conditions at upstream and downstream for the shifted Maxwellians in the direct integration of the Boltzmann equation consists of the following.

$$f_u = \frac{\rho_u}{(\pi T_u)^{3/2}} \exp[-(\xi_1 - \sqrt{5/6} M_u)^2 - \xi_2^2 - \xi_3^2] \quad (X/\lambda \rightarrow -\infty) \quad (18)$$

$$f_d = \frac{\rho_d}{(2\pi T_d)^{3/2}} \exp\{-[(\xi_1 - \sqrt{5/6} M_d)^2 + \xi_2^2 + \xi_3^2] T_u/T_d\} \quad (X/\lambda \rightarrow +\infty) \quad (19)$$

where ρ_d, M_d, T_d (Table 1) are given by the Rankine-Hugoniot relations:

$$\rho_d = \frac{4M_u^2}{(M_u^2 + 3)} \rho_u \quad (20)$$

$$M_d = \left(\frac{M_u^2 + 3}{5M_u^2 - 1} \right)^{1/2} \quad (21)$$

$$T_d = \frac{(5M_u^2 - 1)(M_u^2 + 3)}{16M_u^2} T_u \quad (22)$$

Scope of numerical simulation

In the present study, the Boltzmann solver¹ was validated with results from Ohwada.¹⁰ Further, the results from the gas kinetic scheme were compared with the benchmark solutions from the Boltzmann equations. The solutions from the Boltzmann equations were obtained for Mach 1.2, 2, 3, 5, and 10 shock waves. Comparisons of the solutions were made for distribution functions and the macroscopic variables with those from Ohwada¹⁰ at Mach 1.2, 2, and 3.

The gas kinetic scheme was used to obtain solutions of the internal structure of the shock waves at Mach 1.2, 3, and 5. The macroscopic parameters from these solutions were compared with those from the Boltzmann equations.

Table 2 summarizes the different cases considered in this study with details of the spatial grid size, time step size, and wall clock time.

A velocity grid resolution study was performed for the Mach 1.2, 5, and 10 shock waves for various grids, the details are shown in Table 3.

Table 2. Different Kinetic Schemes Argon Hard Sphere Collision Model

Mach No	Kinetic Scheme	Spatial Grid Size	Time Step Size Transport	Time Step Size Collision	Wall Clock Time/unit computational time/spatial grid pt (mins)	Wall Clock Time (mins)	Comparison with
1.2	Direct Integration of Boltzmann eqn	300	0.01	0.005	0.203	300	Ohwada ¹⁰
1.2	Gas Kinetic BGK	198	-	-	-	0.01	Ohwada ¹⁰
2	Direct Integration of Boltzmann eqn	120	-	-	0.250	120	Ohwada ¹⁰
3	Direct Integration of Boltzmann eqn	120	-	-	0.250	120	Ohwada ¹⁰
3	Gas Kinetic BGK	198	-	-	-	0.01	Ohwada ¹⁰
5	Direct Integration of Boltzmann eqn	110	0.005	0.00125	2.63	110	-
5	Gas Kinetic BGK	198	-	-	-	0.05	Present
10	Direct Integration of Boltzmann eqn	110	0.005	0.005	6.45	50	-

Notes: (1) Wall clock time is based on 3.2 GHz, single Xeon processor
(2) Time step size is normalized as, $\tau_u = \lambda/v_u$, $v_u = \sqrt{kT_u/m}$; subscript u indicates freestream

Table 3. Velocity grid resolution for direct integration of Boltzmann equations

Mach No	Velocity Grid Size (Coarse)	Velocity Grid Size (Fine)	Points in Upstream Peak (Coarse/Fine)	Ratio: max velocity spread upstream and downstream Maxwellians	Radius of velocity sphere (coarse)	Radius of velocity sphere (fine)	Width of velocity bin (fine)
1.2	16x8x8	30x15x15	7/13	0.915	8.262	6.639	0.344
5	14x7x7	20x10x10	3/5	0.339	18.07	14.34	1.43
10	24x12x12	30x15x15	3/5	0.176	28.17	25.82	1.72

Numerical scheme

The system of equations given by Eqn 4 is solved for the N_0 velocity nodes by the conservative splitting method proposed by Tcheremissine.¹ The time step size, $\delta t = t^{j+1} - t^j$. The two-step finite difference scheme for the free transport and the collisions consists of:

$$\frac{\partial f_\gamma}{\partial t} + \xi_\gamma \frac{\partial f_\gamma}{\partial x} = 0 \quad (23)$$

$$\frac{\partial f_\gamma}{\partial t} = I_\gamma \quad (24)$$

Eqn. 23 is approximated by the second-order accurate explicit conservative scheme given in Ref. 15 with the time step governed by the following¹⁵

$$\left| \xi_1 \frac{\delta t}{\delta x} \right| < \frac{1}{2} \quad (25)$$

The time step in Eqn. 24 is governed by the collision frequency which can be the more restrictive of the two. The time step sizes for various Mach numbers in the numerical integration of the equations are given in Table 2. When the

velocity grid is modified, the time step may also require adjustment. Maintaining a fixed value of ratio=(number of integration nodes)/(number of velocity nodes) x (time step size) guides the necessary modification.

Results and Discussions

Results are presented in three sections for solutions of the internal structure of shock waves of a monatomic gas with the hard sphere collision model. The first section presents validation of a Boltzmann solver¹ with a reference Boltzmann solver¹⁰ for Mach numbers of 1.2, 2, and 3. The second section presents effects of velocity grid resolution on the solutions from the Boltzmann solver¹ for Mach 1.2, 5, and 10. The third section addresses accuracy issues of a recently developed multi-temperature model in a gas kinetic scheme^{8,9} for Mach 1.2, 3, and 5. For the results shown in the subsequent sections, the distance along the shock wave is normalized by the upstream mean free path. The macroscopic parameters consist of normalized streamwise velocity, density, temperature, streamwise and normal components of temperature, the xx-component of viscous stress, and the streamwise component of heat transfer. Two forms of the distribution function were used as deemed appropriate: Distribution function, $f=f(x, \xi_1, \xi_2)$, and the probability distribution function, $\mathcal{P} = f(x, \xi_1, \xi_2)/\rho$. The distribution function, f was normalized by its highest value in some cases for proper graphical representation.

Validation of Boltzmann solver

The process of validation of the present Boltzmann solver consisted of comparing the distribution function and macroscopic parameters with those of the Ohwada¹⁰ solution. Figs. 1 and 2 show comparisons of macroscopic parameters of a Mach 1.2 shock wave in a monatomic gas with the hard sphere collision model. The relatively small jumps of the macroscopic parameters across the shock wave are noted for this Mach number, (see Table 1). However, the thickness of the shock wave extends across nearly sixty mean free paths. Consequently, one notes the longer total wall clock time for the relatively larger time steps in the free transport and collisions parts of the Boltzmann solver (Table 2). There is excellent agreement of the present solutions for both Mach 1.2 and 2 with the reference solutions of density, temperature, the xx-component of viscous stress (P_{11}). However, the present computation overpredicts the streamwise peak heat transfer ($-Q_1$) from Ohwada's for the Mach 1.2 shock wave by about 6%.

Fig. 3 shows a qualitative comparison of the distribution function, $f(x, \xi_1, \xi_2)$ of the current Boltzmann solution with Ohwada's for a Mach 3 shock wave. It is noted that spatial coincidence of distributions was optimized. The Mach 3 shock thickness is approximately fifteen mean free paths. The asymptotic form of the distribution function is a shifted Maxwellian prescribed by the Rankine-Hugoniot conditions (Table 1). The Mach number reduces from the upstream to downstream across the shock by a factor of 5.74. One can see from the figure that there are relatively small deviations from the asymptotic distribution in the upstream and downstream locations Fig.3a and d. For the locations inside the shock front, Fig.3b and c, reduction of the mean velocity and the shock heating lead to non-Maxwellian distributions. There is good qualitative agreement of the present Boltzmann solution with reference at all four x locations.

Fig. 4 shows the magnitude of $f(x, \xi_1, \xi_2)$ at $x/\lambda = -0.6$ for four ξ_2 - velocities. This x -location is slightly upstream of the center of the shock wave, the distribution is non-Maxwellian due to heating. There is good agreement of the present computation with Ohwada's. Consequently, the macroscopic parameters of the Mach 3 shock wave (Fig. 5) also show agreement. Fig. 5 shows comparisons of velocity, density, temperature, xx-component of viscous stress, and the streamwise component of the heat flux. Comparison of the Mach 3 shock wave solution with that of the Mach 1.2, shows that shock thickness reduces by about 50%, the viscous stress increases by a factor of 60 and the heat flux increases by a factor of 160. The total wall clock time of the Mach 3 shock wave decreases by about 50% to that of the Mach 1.2 shock wave (Table 2).

Distribution functions inside the shock wave

Prior to the discussion of the effects of the velocity grids, the distribution functions normalized by their respective peak values at four x -locations are presented for Mach 1.2, 5 and 10 in Figs. 6 to 8. The spatial locations are, far upstream, slightly upstream of center of shock, slightly downstream of center location, and far downstream. The asymptotic form of the distribution function at the upstream and downstream is given by the shifted Maxwellian prescribed by the Rankine-Hugoniot conditions. With increase in Mach number, Figs. 7 and 8, one sees a greater shock heating, leading to non-Maxwellian distribution at $x/\lambda = 0.0$ and a bimodal distribution at $x/\lambda = 0.8$. Increases in Mach number

causes greater ξ_1 -velocity shifts from upstream to downstream in the distribution function; in addition, one sees an increase in ξ_1 -velocity spread in the downstream distribution function, 5, 15, and 20 ξ_1 -velocities for Mach 1.2, 5, and 10 respectively. The upstream distribution function is spread over ξ_1 -velocities (normalized by $\sqrt{\frac{2kT_u}{m}}$) of 5, 5, and 10 for Mach 1.2, 5, and 10, respectively.

Effect of velocity grid resolution on Boltzmann solver

A velocity grid resolution study was conducted with five different velocity grids at Mach numbers of 1.2, 5, and 10. See Table 3 for details. The velocity grid with a size of 30x15x15, for Mach 1.2 as an example, has 30 nodes in the streamwise direction, and 15 nodes in the two normal directions, with a total of 6750 nodes. In the results to follow, the smallest velocity grid on which the macroscopic parameters converged is labeled the fine grid and the grid with total number of nodes smaller than this is considered the coarse grid. It is noted that to assess the effect of the velocity grid size on the numerical solution, one would not only consider the evaluation of the distribution function on the given velocity nodes, but also the resolution of the velocity nodes in representing the distribution function, which in turn determines the predictive accuracy of the macroscopic parameters. Table 3 gives details of velocity grid resolution, such as the grid, number of points in the upstream distribution, and radius of the velocity sphere.

Mach 1.2

Fig. 9a and b show the density and heat flux profiles in the Mach 1.2 shock wave for five different velocity grids considered in the study. One may note from the Table 3 that the velocity bin size is given by the radius of the velocity sphere and the number of grid points. The variation of density for different grids is not significant. The heat flux which represents higher moments of the distribution function shows more significant deviations with changes in velocity grid sizes. The velocity grids of 30x15x15, 24x12x12, 20x10x10, and 18x9x9 result in minor deviations from the fine grid result whereas, the lowest grid density of 16x8x8 shows significant departure in the peak value and at the far upstream and downstream locations. The reasons for the failure of the coarse velocity grids is discussed further.

Fig. 10 shows the variation of the streamwise component of the temperature in the Mach 1.2 shock wave. For both the velocity grids depicted (30x15x15 and 16x8x8), the variation in streamwise temperature is insignificant at this Mach number.

Fig. 11 shows the probability distribution functions at three different locations in the Mach 1.2 shock wave. One may note the significant alteration of the magnitude and shape of the distribution function due to the coarse grid. The lack of grid resolution in the coarse grids to properly represent the shape of the distribution function is attributed to the large deviation in heat flux shown earlier in Fig. 9b.

Mach 5 and 10

Fig. 12 shows profiles of macroscopic parameters in the Mach 5 shock wave. With the increase in Mach number, there is a greater effect of coarse grid on the lower as well as higher moments of the distribution function, shown in the figure of density and heat flux, respectively. The coarse grid underpredicts the density in the upstream and downstream locations. It is noted that the Rankine-Hugoniot conditions (Table 1) are properly enforced for all the grids with the density profiles shown in Fig. 12a. The effect of the coarse grid on the heat flux is to shift the peak location slightly upstream and a lower heat flux in the upstream region.

Fig. 13 shows the streamwise temperature profile in the Mach 5 shock wave for two different velocity grids. The coarse grid has the effect of underpredicting the heat flux in the upstream and overpredicting at the downstream locations. This under- and over-predictions are a consequence of the differences in shapes and magnitudes of the probability distribution functions for the coarse and fine grids shown in Fig. 14. It is seen that the relative magnitudes of the peaks due to coarse and fine grids are significantly different in the shock wave (Fig. 14a and b) and close to each other far downstream (Fig. 14c).

The results for the effect of velocity grid resolution on macroscopic parameters and the distribution function for the Mach 10 shock wave are qualitatively the same as Mach 5, shown in Figs. 15 to 17. However, the coarse grids have a greater effect on the accuracy of the Mach 10 solution than the Mach 5. One notes that, as before, the Rankine-Hugoniot conditions (Table 1) are properly enforced for all the grids with the density profiles shown in Fig. 15a.

It is important to note that the velocity grid considered above was based on convergence of the macroscopic flow variables. The accurate representation of the distribution function, however, will require still finer velocity grids, as shown in the next figure. Fig. 18 presents the probability distribution function for two different velocity grids for a Mach 5 shock wave. The two velocity grids considered are 30x15x15 (coarse) and 60x30x30 (fine). The grid size of

30x15x15 was found to be adequate for the accurate prediction of macroscopic quantities, but as seen from the figure, the 60x30x30 velocity grid has an enhanced resolution of the distribution function.

In conclusion, one notes that with increase in Mach number there is a greater need for grid resolution, particularly in the upstream peak of the velocity distribution function. However, at the lower Mach number, the velocity grid requirements depend on the ratio of the spread of the velocity distribution functions at the upstream and downstream locations. See Table 3. Velocity grid resolution affects the prediction of the macroscopic parameters as follows, (1) the effect on the evaluation of the distribution function on a given node, (2) the effect on the evaluation of the moments of the distribution function. Delineating the relative effects of the two provides useful criteria for optimizing the size of the velocity grids in Boltzmann solvers, which is a subject of future research.

Representation of the distribution function with analytic function

This section presents an attempt to represent the distribution function in the Mach 5 shock wave analytically by superposition of the upstream and downstream Maxwellian distributions using the information of the solution of the Boltzmann equation. Assume $f(\xi_1)$, the distribution function, can be written as the linear combination of $f_u(\xi_1)$ and $f_d(\xi_1)$, where $f_u(\xi_1)$ is the drifting Maxwellian distribution upstream of the shock wave with density ρ_u , temperature, T_u , and freestream velocity of u_u . Likewise, the drifting Maxwellian distribution downstream of the shock wave is $f_d(\xi_1)$ with density ρ_d , temperature, T_d , and velocity of u_d .

$$f(\xi_1) = af_u(\xi_1) + bf_d(\xi_1) \quad (26)$$

where a, b are determined at each value of the spatial distance x.

$$f(\xi_1, x) = a(x)f_u(\xi_1) + b(x)f_d(\xi_1) \quad (27)$$

If we evaluate f at u_u and u_d , the pre- and post-shock freestream velocities, we can determine a and b . Denoting $\xi_1 = u_u$ and $\xi_1 = u_d$,

$$f(u_u, x) = a(x)f_u(u_u) + b(x)f_d(u_u) \quad (28)$$

$$f(u_d, x) = a(x)f_u(u_d) + b(x)f_d(u_d) \quad (29)$$

We can now evaluate, $a(x)$ and $b(x)$ as follows.

$$a(x) = \left(\frac{\frac{f(u_d, x)}{f_d(u_d)} - \frac{f(u_u, x)}{f_d(u_u)}}{\frac{f_u(u_d)}{f_d(u_d)} - \frac{f_u(u_u)}{f_d(u_u)}} \right), \quad b(x) = \left(\frac{\frac{f(u_d, x)}{f_u(u_d)} - \frac{f(u_u, x)}{f_u(u_u)}}{\frac{f_d(u_d)}{f_u(u_d)} - \frac{f_d(u_u)}{f_u(u_u)}} \right) \quad (30)$$

Fig. 19 presents the distribution function obtained from the weighted superposition of the upstream and downstream Maxwellian distributions, the coefficients obtained from the above-mentioned analytic function. This distribution is compared with the true distribution function obtained from the solution of the Boltzmann equation. The agreement of the two distribution functions is very good. At $x/\lambda = 0$, there is small variation of the contour in the blended distribution function from $\xi_1=0$ to 4 near $\xi_2=0$. Possible speed-ups in computational load can be achieved by using the analytic function in specifying more realistic initial and boundary conditions in kinetic schemes.

An ellipsoidal distribution can be seen in the middle of the shock wave (Fig. 19b). This distribution was used (recall from the Analysis section presented earlier) to construct the multi-temperature model of the gas kinetic BGK scheme, the results of this scheme described next.

Accuracy of gas kinetic scheme

Mach 1.2, 3, and 5

Figs 20 to 23 show the comparison of the macroscopic parameters of the gas kinetic scheme with the solutions of the Boltzmann equation for the Mach 1.2, 3, and 5 shock waves with hard sphere collision model. The profiles of density, streamwise and normal components of temperature are shown for Mach 1.2 (Fig. 20). For Mach 3, Fig. 21, the profiles shown for density, temperature, viscous stress (xx-component) and streamwise component of heat flux. The agreement of the present results of the gas kinetic scheme with reference (Ohwada's¹⁰) solution at Mach 1.2 and 3 are evident. One may conclude that the three kinetic schemes (present Boltzmann and gas kinetic and Ohwada's) give good agreement of macroscopic parameters for Mach 1.2 to 3 shock waves.

The effect of variation of Prandtl number on the gas kinetic BGK scheme is shown in Fig. 22. It is noted that as the Prandtl number is reduced, the shock front migrates upstream, more apparent in the temperature profiles. Fig. 23 shows the density, mean temperature, and the streamwise and normal temperatures for the present gas kinetic scheme and the Boltzmann solution for the Mach 5 shock wave. From the comparison of the density profiles, Fig. 23a, one notes the excellent match of the density profiles for the Mach 5 shock wave. However one notes from Fig. 23b and c that the starting location of the prediction of the temperatures by the gas kinetic scheme is more upstream than that of the Boltzmann solution. The discrepancy between the two kinetic schemes is a subject of further investigation.

CONCLUDING REMARKS

A numerical study was performed for the solution of the internal structure of shock waves in monatomic gas using two different kinetic methods, assuming the hard sphere collision model. A velocity grid resolution study of a Boltzmann solver was conducted for Mach numbers of 1.2, 5, and 10. Macroscopic parameters and the distribution function predicted in the present study for Mach 1.2 to 3 shock waves agree well with those of Ohwada's. Velocity grid requirements for the accurate prediction of the macroscopic parameters from the solution of the Boltzmann equation are reported in the present study. From the solution of the Boltzmann equation, an analytic function was developed that can be used in computationally efficient kinetic methods, such as the gas kinetic schemes to represent realistic physics.

Detailed numerical simulations were performed with a gas kinetic BGK scheme and a direct integration method of Boltzmann equation to analyze the translational nonequilibrium phenomena that arise in hypersonic aerodynamic flows. A multi-translational temperature gas kinetic model based on anisotropy of the velocity distribution function for monatomic gas shock structures was compared with direct integration of Boltzmann equation solutions. The agreement of the gas kinetic BGK method was excellent at low Mach numbers and there was improper prediction of upstream location at the Mach number of five, a subject of future investigation. In the nonequilibrium regions where the assumptions are valid, the gas kinetic BGK scheme provides very high level of computational efficiency suitable for hypersonic flow calculations.

ACKNOWLEDGEMENTS

Partial support by U.S. Air Force Office of Scientific Research contract monitored by F. Fahroo. Authors are grateful to F. G. Tcheremissine for providing the numerical method of the direct integration of Boltzmann equation.

References

- ¹F.G. Tcheremissine. Solution of the Boltzmann Kinetic Equation for High-Speed Flows. *Computational Mathematics and Mathematical Physics*, 46(2):315–329, 2006.
- ²P. Degond, L. Pareschi, and G. Russo. *Modeling and Computational Methods for Kinetic Equations*. Series on Modeling and Simulation in Science, Engineering & Technology, Birkhauser, Boston, 2004.
- ³N. Bellomo and R. Gatignol. *Lecture Notes on the Discretization of the Boltzmann Equation*. Series in Advances in Mathematics for Applied Sciences, 63, World Scientific Publishing Co., River Edge, NJ, 2003.
- ⁴V.V. Aristov. *Direct Methods for Solving the Boltzmann Equation and Study of Non-Equilibrium Flows Phenomena*. Kluwer Academic Publishers, Dordrecht, 2001.
- ⁵C. Cercignani. *Boltzmann Equation And Its Applications*. Springer-Verlag, New York, 1988.
- ⁶E. Josyula and W.F. Bailey. Vibrational Population Enhancement in Nonequilibrium Dissociating Hypersonic Nozzle Flows. *Journal of Thermophysics and Heat Transfer*, to appear in 2004.
- ⁷K. Xu and E. Josyula. Multiple Translational Temperature Model and its Shock Structure Solution. *Physical Review E*, 71:056308(1–5), 2005.
- ⁸E. Josyula, K. Xu, and D.C. Wadsworth. Testing Continuum and Non-Continuum Descriptions in High Speed Flows. In *Rarefied Gas Dynamics: 24th International Symposium*, volume CP762, New York, 2005. American Institute of Physics.
- ⁹K. Xu and E. Josyula. Continuum Formulation for Non-Equilibrium Shock Structure Calculation. *Communications in Computational Physics*, 1(3):425–448, June 2006.
- ¹⁰Taku Ohwada. Structure of Normal Shock Waves: Direct Numerical Analysis of the Boltzmann Equation for Hard-Sphere Molecules. *Physics of Fluids A*, 5(1):271–234, January 1993.
- ¹¹K. Xu. Regularization of the Chapman-Enskog Expansion and its Application of Shock Structure. *Physics of Fluids*, 14(4):L17–L20, 2002.
- ¹²P.L. Bhatnagar, E.P. Gross, and M. Krook. A Model for Collision Processes in Gases I: Small Amplitude Processes in Charged and Neutral One-Component Systems. *Phys. Rev.*, 94:511–525, 1954.

¹³K. Xu. A Gas-Kinetic BGK Scheme for the Navier-Stokes Equations and its Connection with Artificial Dissipation and Godunov Method. *Journal of Computational Physics*, 171:289–335, 2001.

¹⁴G.V. Candler, S. Nijhawan, and D. Bose. A Multiple Translational Temperature Gas Dynamics Model. *Physics of Fluids*, 6(11):3776–3786, November 1994.

¹⁵J.P. Boris and D.L. Book. Flux Corrected Transport. I. SHASTA A Fluid Transport Algorithm that Works. *Journal of Computational Physics*, 11:38–69, 1973.

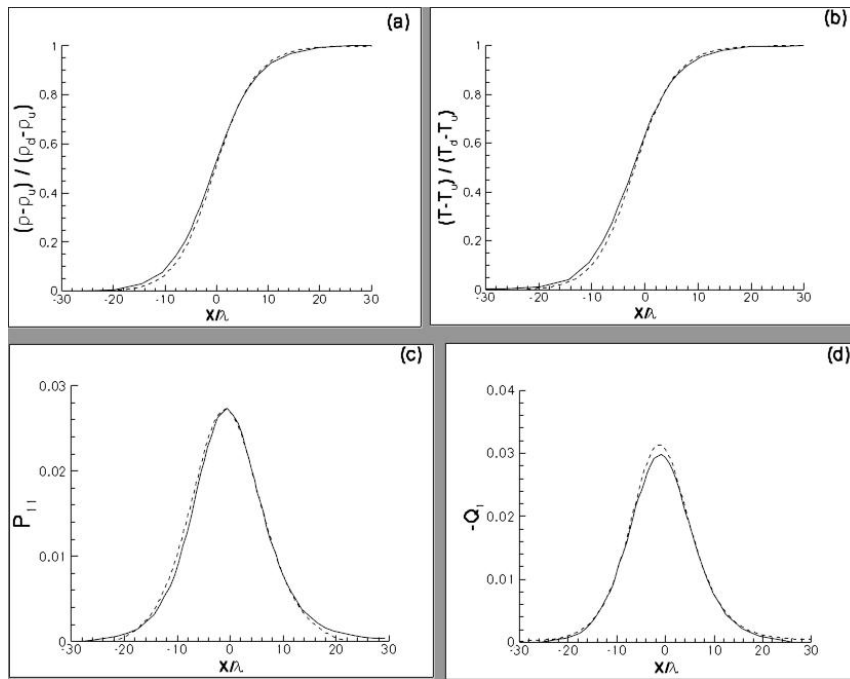


Figure 1. Macroscopic parameters in Mach 1.2 shock wave with hard sphere collision model, (a) density, (b) temperature, (c) viscous stress xx-component, (d) heat flux in x-direction. - - - - - Boltzmann (Present) _____ Boltzmann (Ohwada)

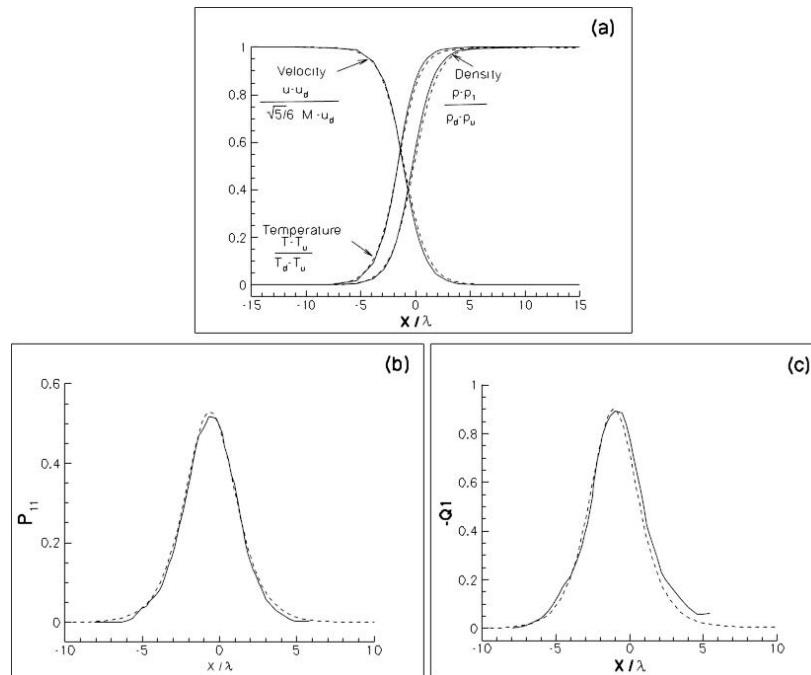


Figure 2. Macroscopic parameters in Mach 2 shock wave with hard sphere collision model, (a) u-velocity, density, and temperature, (b) viscous stress xx-component, (c) heat flux in x-direction. - - - - - Boltzmann (Present) _____ Boltzmann (Ohwada)

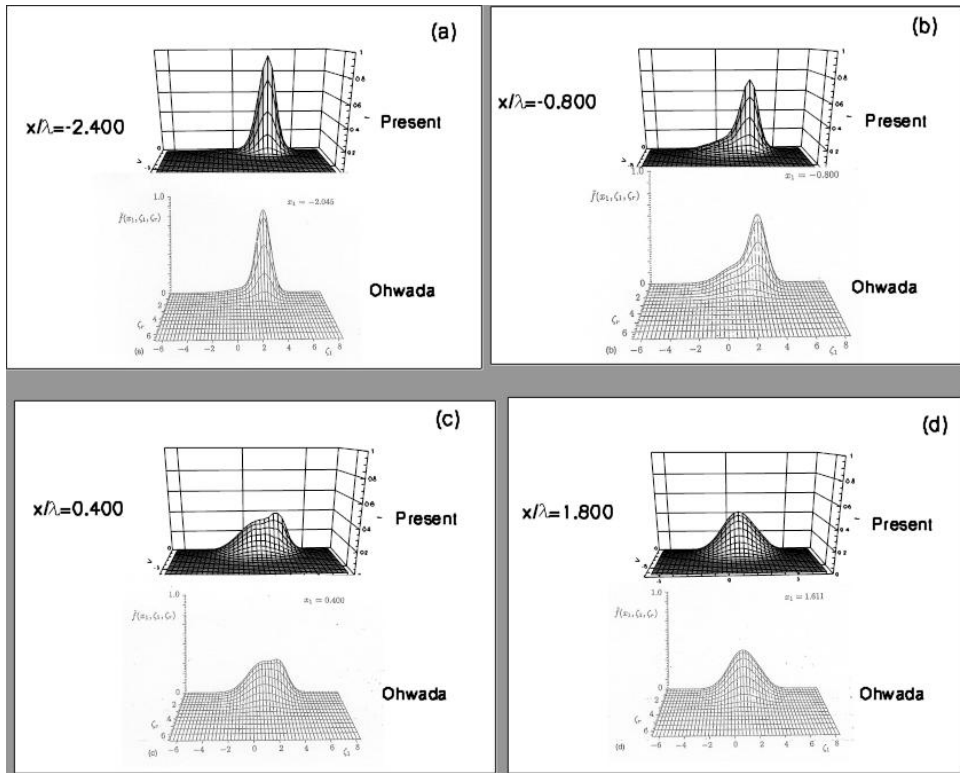


Figure 3. Distribution function in Mach 3 shock wave with hard sphere collision model, (a) $x/\lambda=-2.4$, (b) $x/\lambda=-0.8$, (c) $x/\lambda=0.4$, (d) $x/\lambda=1.8$

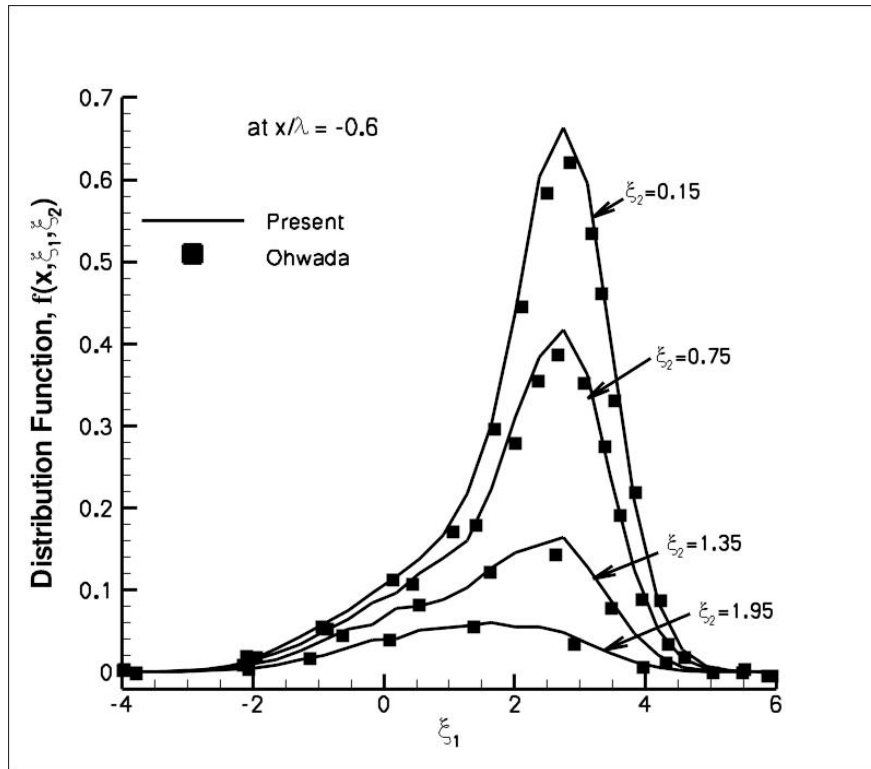


Figure 4. Distribution function in Mach 3 shock wave for different ξ_2 -velocities with hard sphere collision model

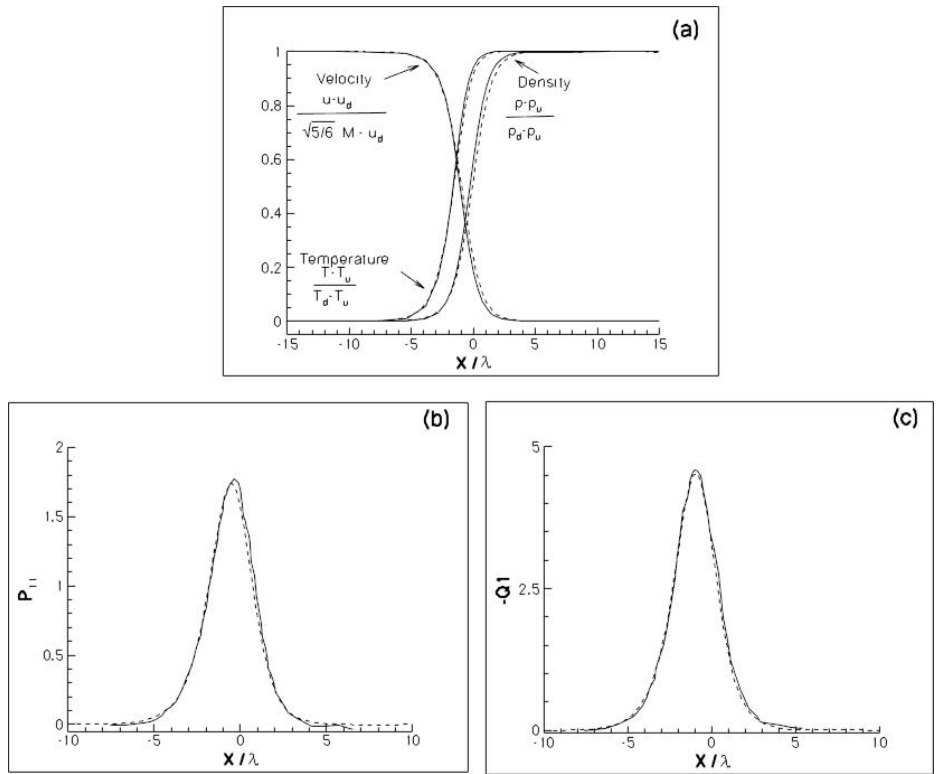


Figure 5. Macroscopic parameters for a Mach 3 shock wave with hard sphere collision model, (a) u-velocity, (b) viscous stress xx-component, (c) heat flux x-component. - - - - - Boltzmann (Present) ——— Boltzmann (Ohwada)

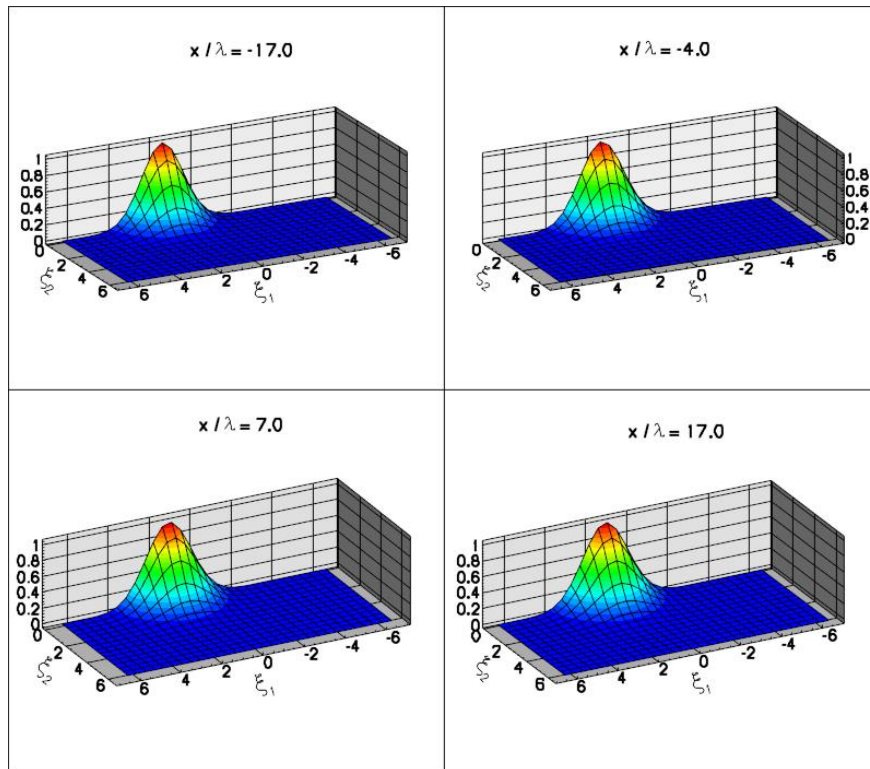


Figure 6. Velocity distribution function inside a Mach 1.2 shock wave with hard sphere collision model, (a) $x/\lambda=-17$, (b) $x/\lambda=-4$, (c) $x/\lambda=7$, (d) $x/\lambda=17$

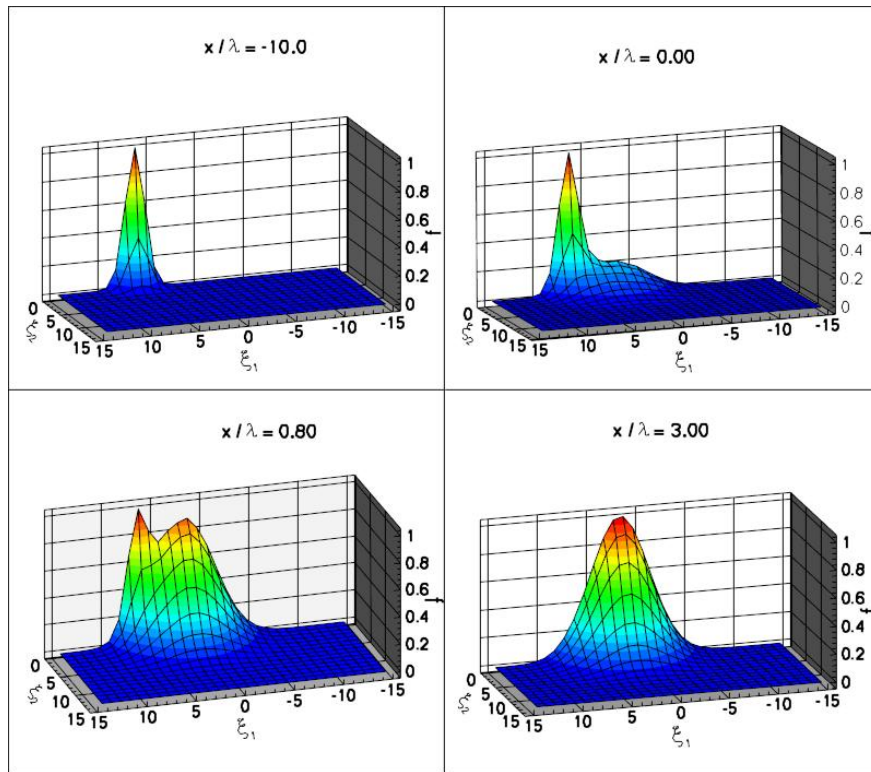


Figure 7. Velocity distribution function inside a Mach 5 shock wave with hard sphere collision model, (a) $x/\lambda = -10$, (b) $x/\lambda = 0$, (c) $x/\lambda = 0.8$, (d) $x/\lambda = 3$

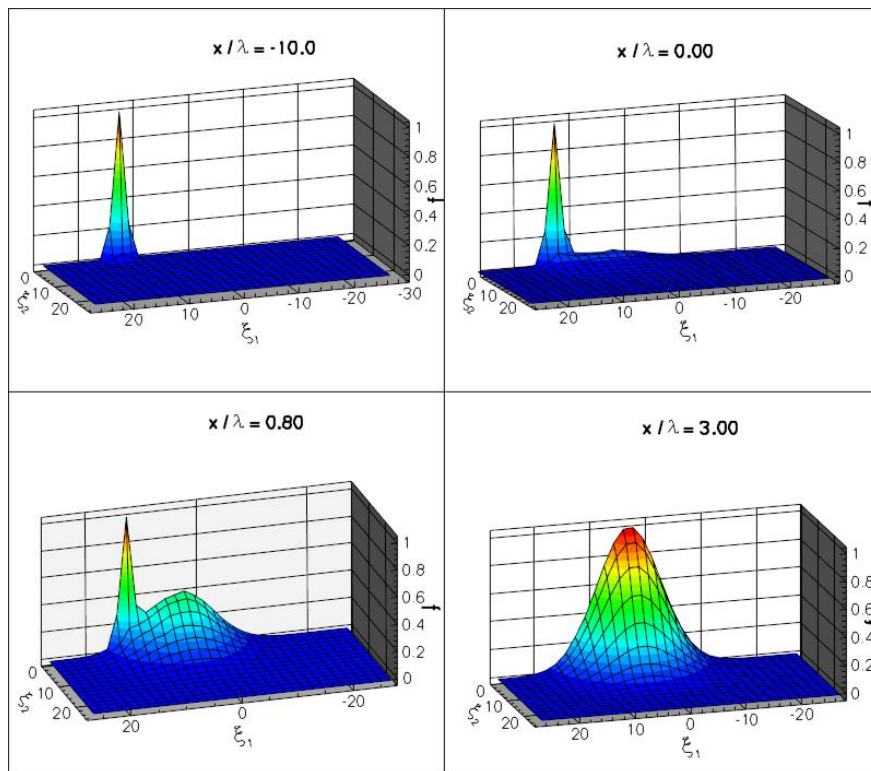


Figure 8. Velocity distribution function inside a Mach 10 shock wave with hard sphere collision model, (a) $x/\lambda = -10$, (b) $x/\lambda = 0$, (c) $x/\lambda = 0.8$, (d) $x/\lambda = 3$

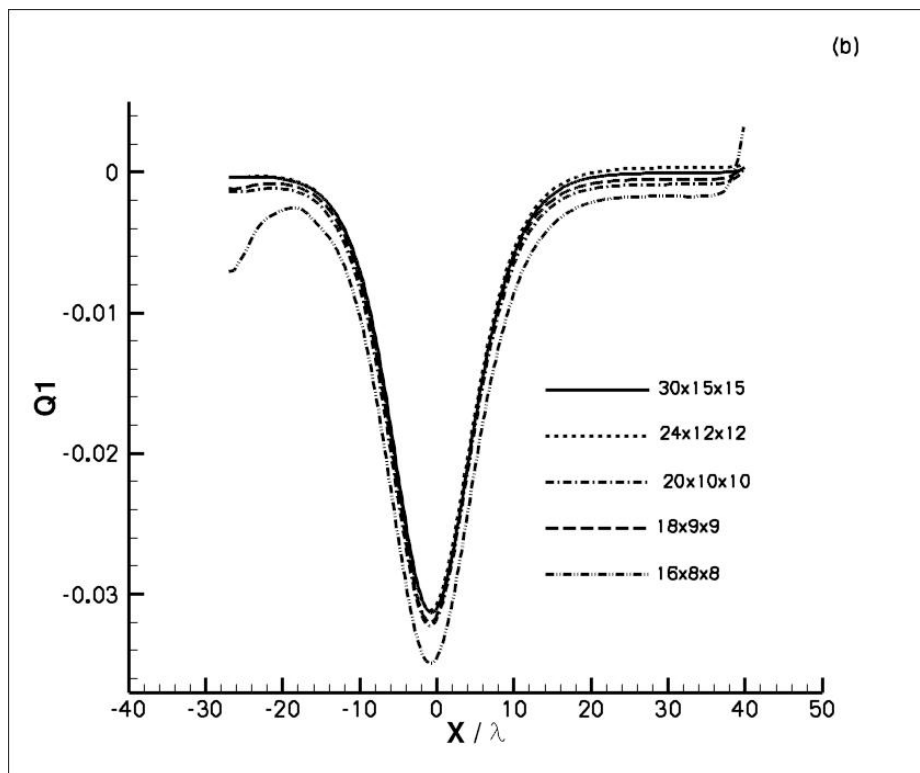
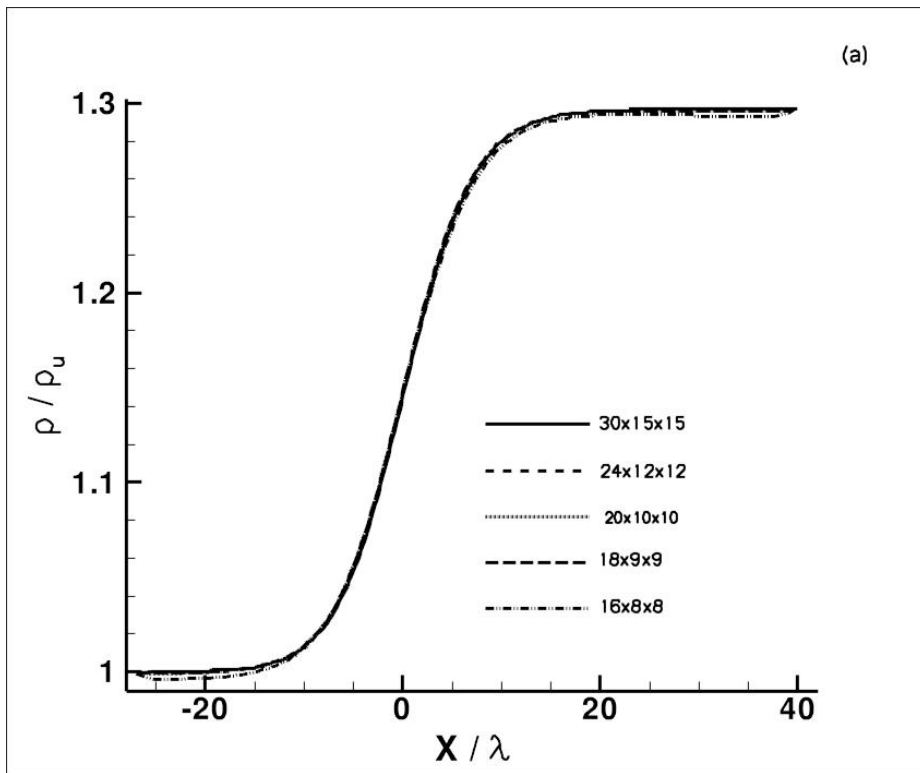


Figure 9. Velocity grid resolution: Macroscopic parameters in a Mach 1.2 shock wave with hard sphere collision model on five different velocity grids, (a) density, (b) heat flux x-component

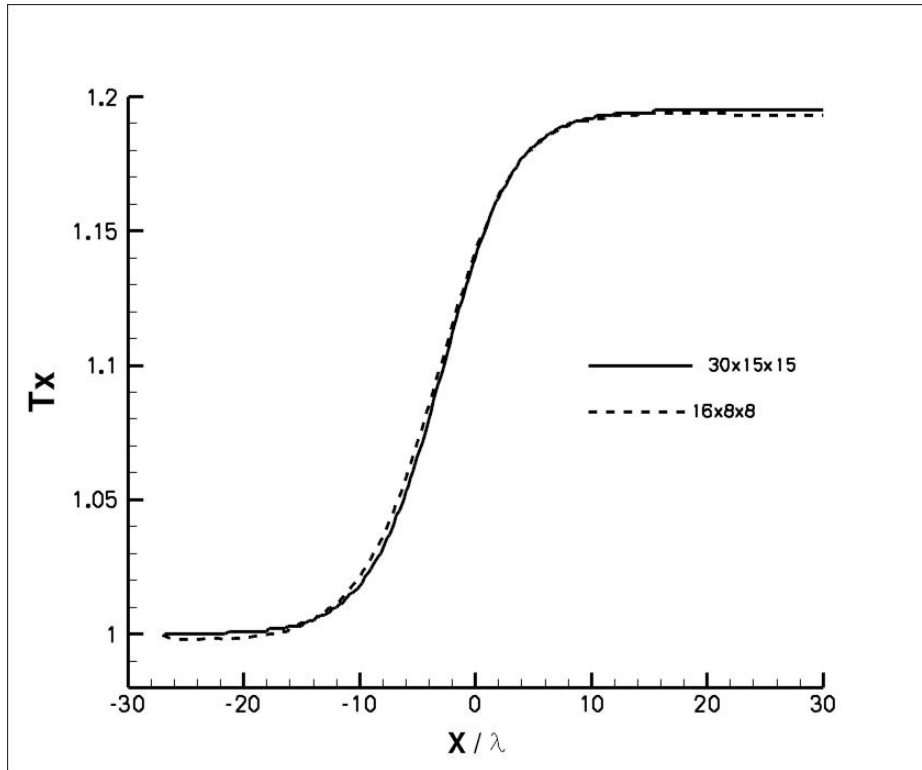


Figure 10. Velocity grid resolution: Streamwise component of temperature in a Mach 1.2 shock wave with hard sphere collision model on two different velocity grids

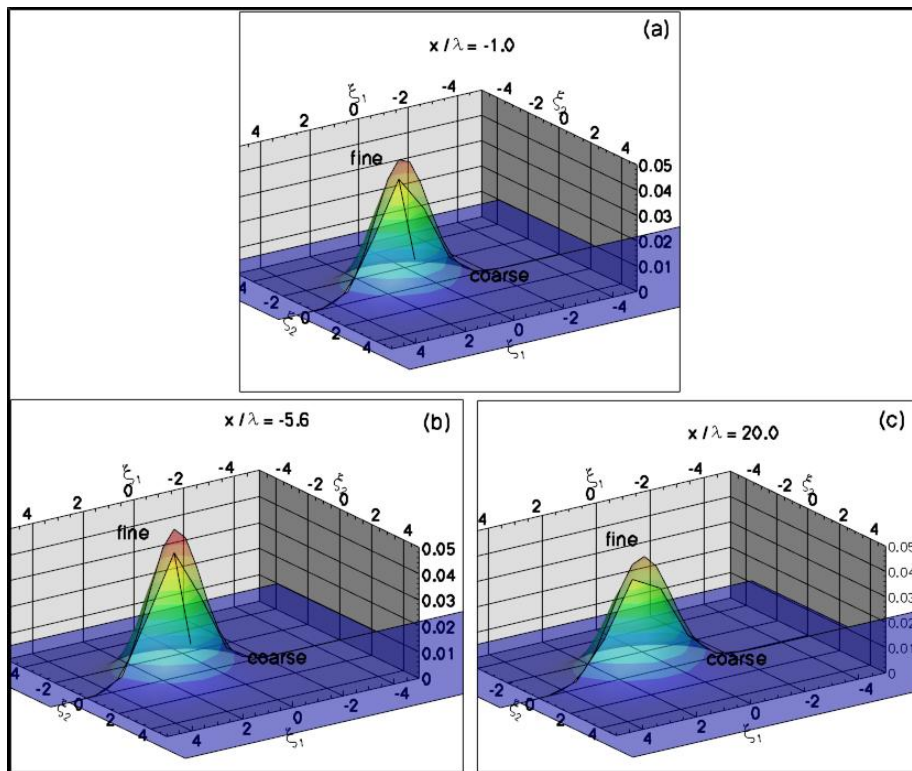


Figure 11. Velocity grid resolution: Probability distribution function in a Mach 1.2 shock wave with hard sphere collision model on coarse and fine grids, (a) $x/\lambda=-1$, (b) $x/\lambda=-5.6$, (c) $x/\lambda=20.0$

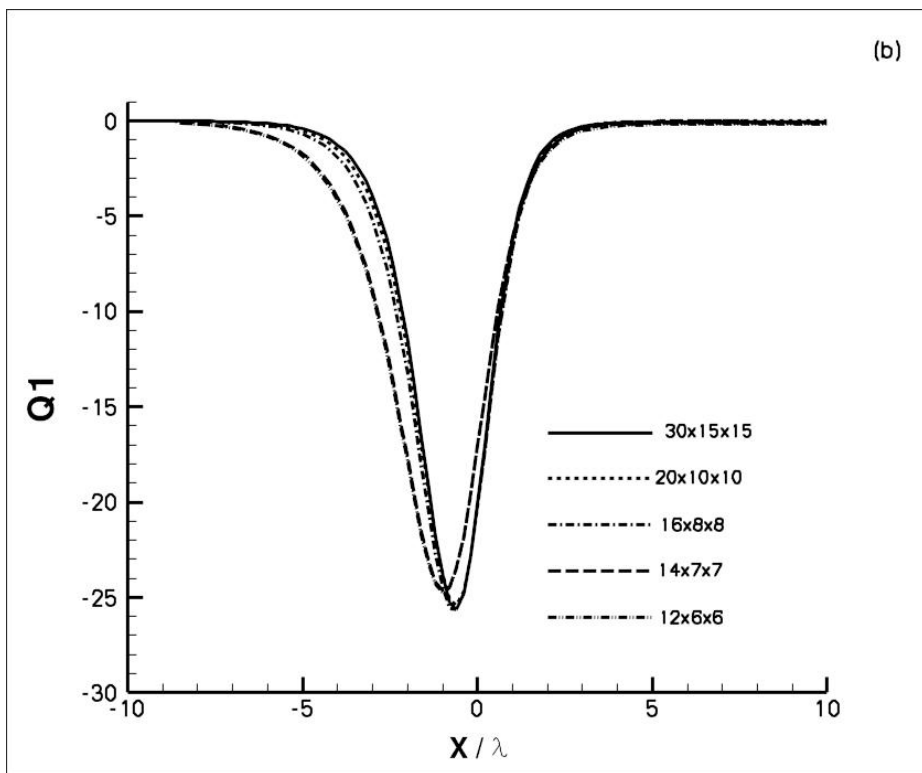
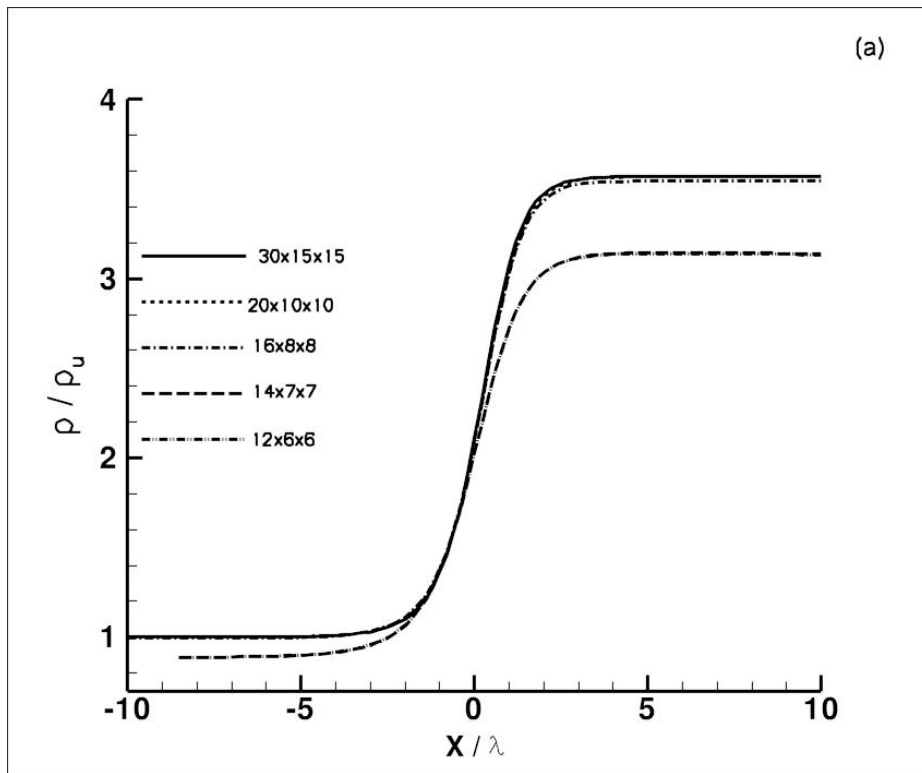


Figure 12. Velocity grid resolution: Macroscopic parameters in a Mach 5 shock wave with hard sphere collision model on five different velocity grids, (a) density, (b) heat flux x-component

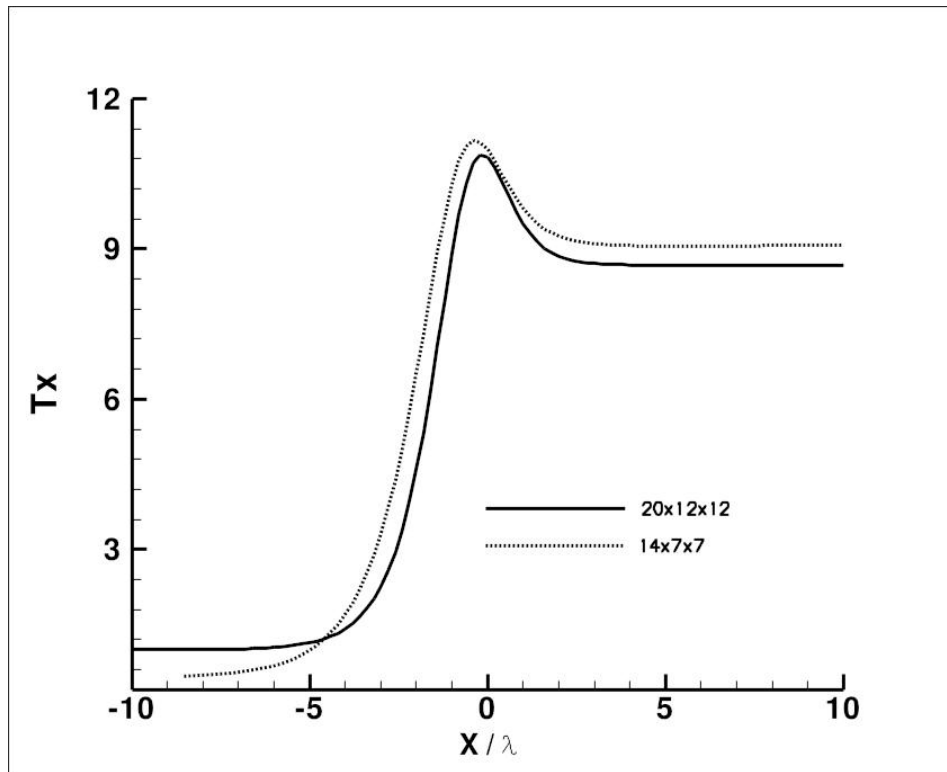


Figure 13. Velocity grid resolution: Streamwise component of temperature in a Mach 5 shock wave with hard sphere collision model on two different velocity grids)

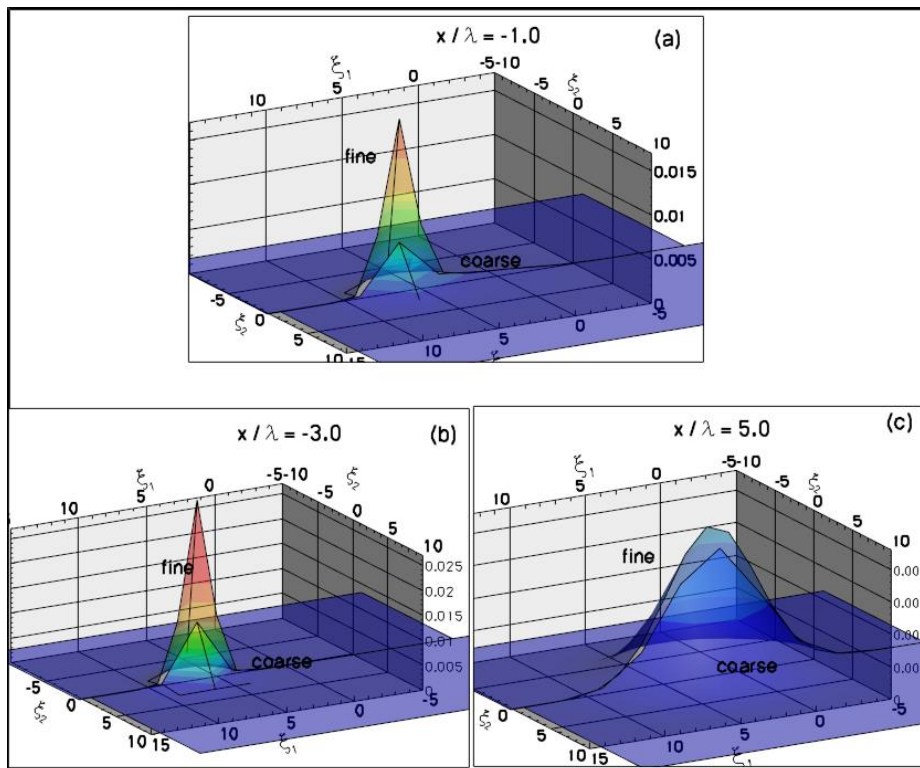


Figure 14. Velocity grid resolution: Probability distribution function in a Mach 5 shock wave with hard sphere collision model on coarse and fine grids, (a) $x/\lambda=-1$, (b) $x/\lambda=-3$, (c) $x/\lambda=5$

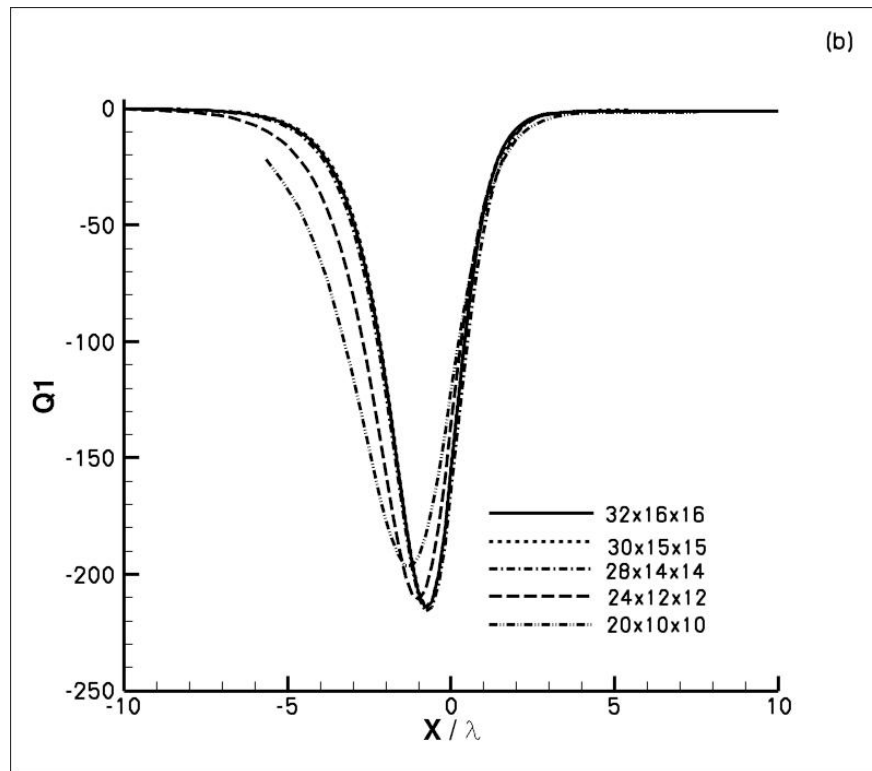
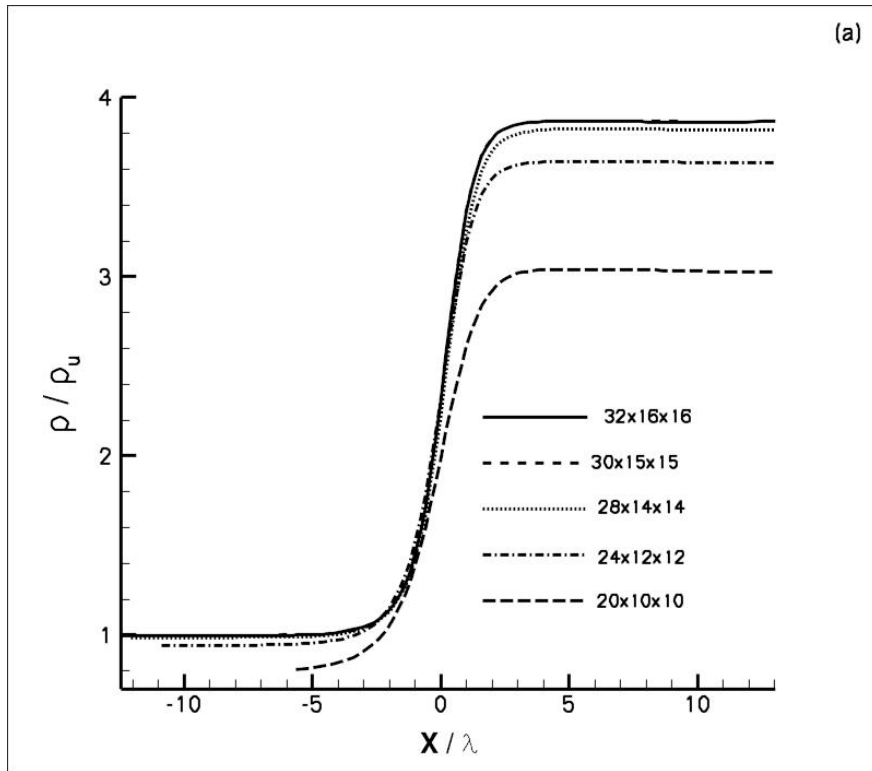


Figure 15. Velocity grid resolution: Macroscopic parameters in a Mach 10 shock wave with hard sphere collision model on five different velocity grids, (a) density, (b) heat flux x-component

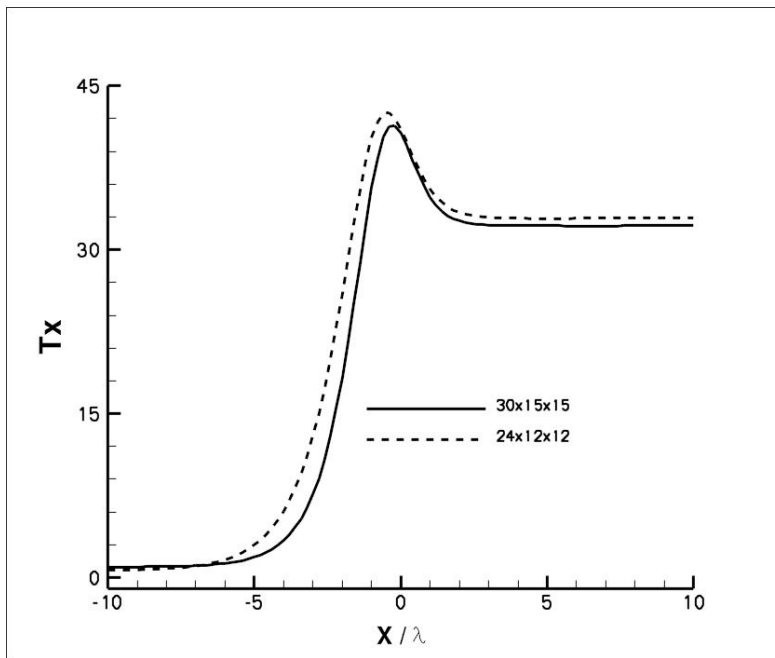


Figure 16. Velocity grid resolution: Streamwise component of temperature in a Mach 10 shock wave with hard sphere collision model on two different velocity grids

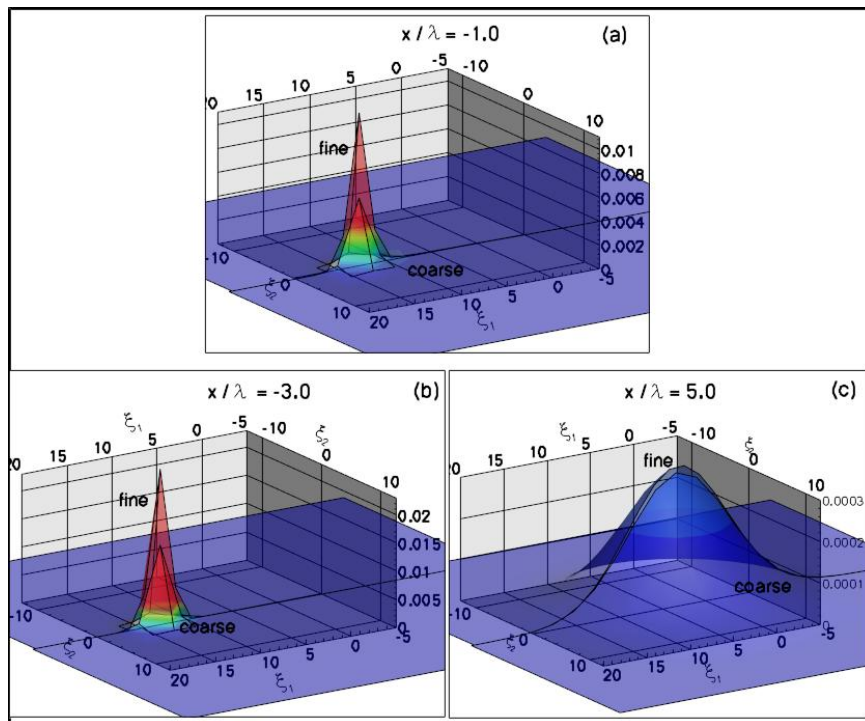


Figure 17. Velocity grid resolution: Probability distribution function in a Mach 10 shock wave with hard sphere collision model on coarse and fine grids, (a) $x/\lambda = -1$, (b) $x/\lambda = -3$, (c) $x/\lambda = 5$

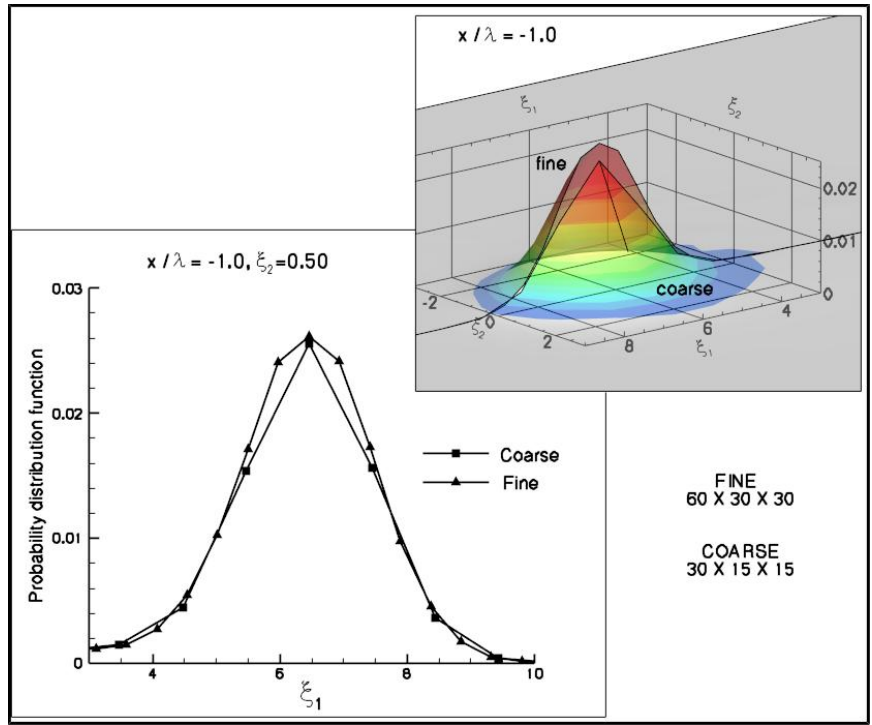


Figure 18. Velocity grid resolution: Probability distribution function in a Mach 5 shock wave with hard sphere collision model on coarse and fine grids, (a) $x/\lambda=-1$, (b) $x/\lambda=-3$, (c) $x/\lambda=5$

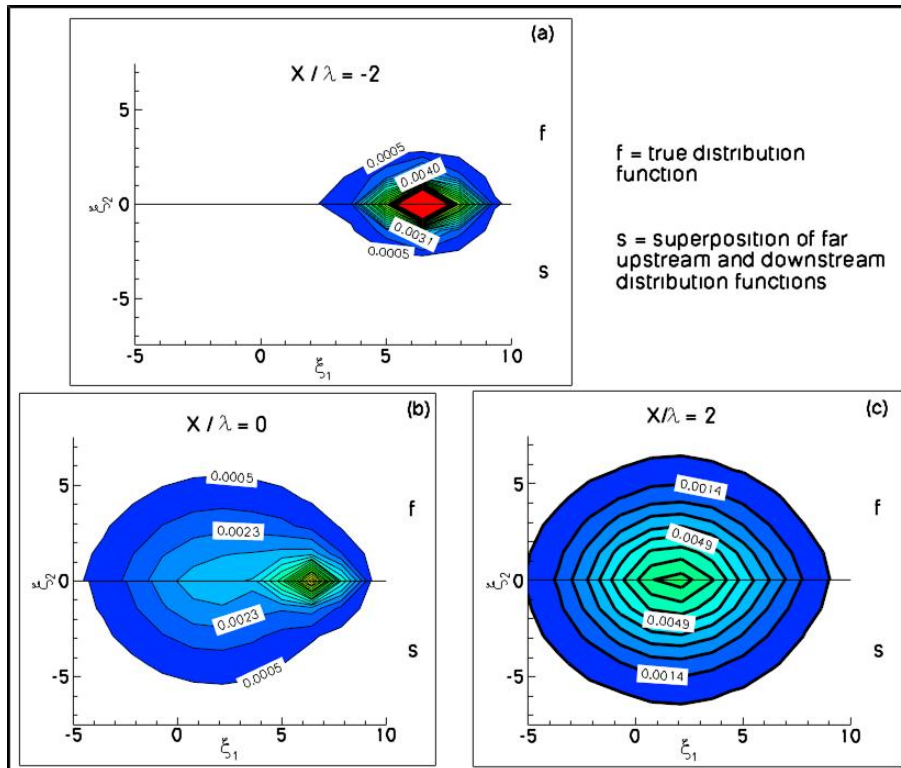


Figure 19. Comparison of true distribution function with blended distribution function in Mach 5 shock wave, (a) $x/\lambda = -2$ (b) $x/\lambda = 0$ (c) $x/\lambda = 2$

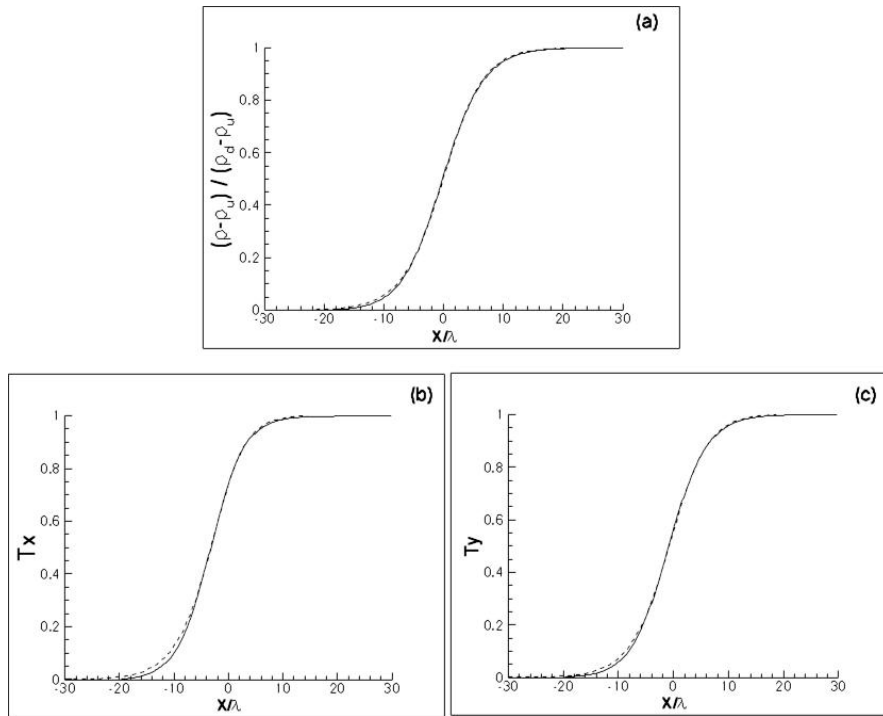


Figure 20. Accuracy of gas kinetic scheme: Macroscopic parameters inside Mach 1.2 shock wave with hard sphere collision model, (a) density, (b) Streamwise component of temperature, (c) Normal component of temperature.
 - - - - - Gas Kinetic Scheme
 _____ Boltzmann (Ohwada)

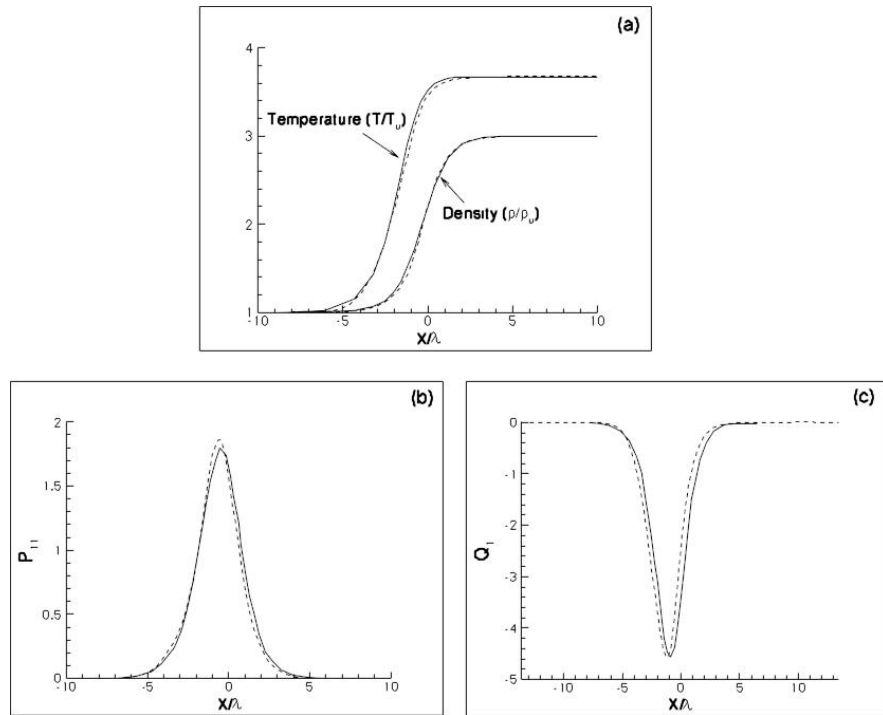


Figure 21. Accuracy of gas kinetic scheme: Macroscopic parameters inside Mach 3 shock wave with hard sphere collision model, (a) density and temperature, (b) viscous stress xx-component, (c) heat flux x-component.
 - - - - - Gas Kinetic Scheme
 _____ Boltzmann (Ohwada)

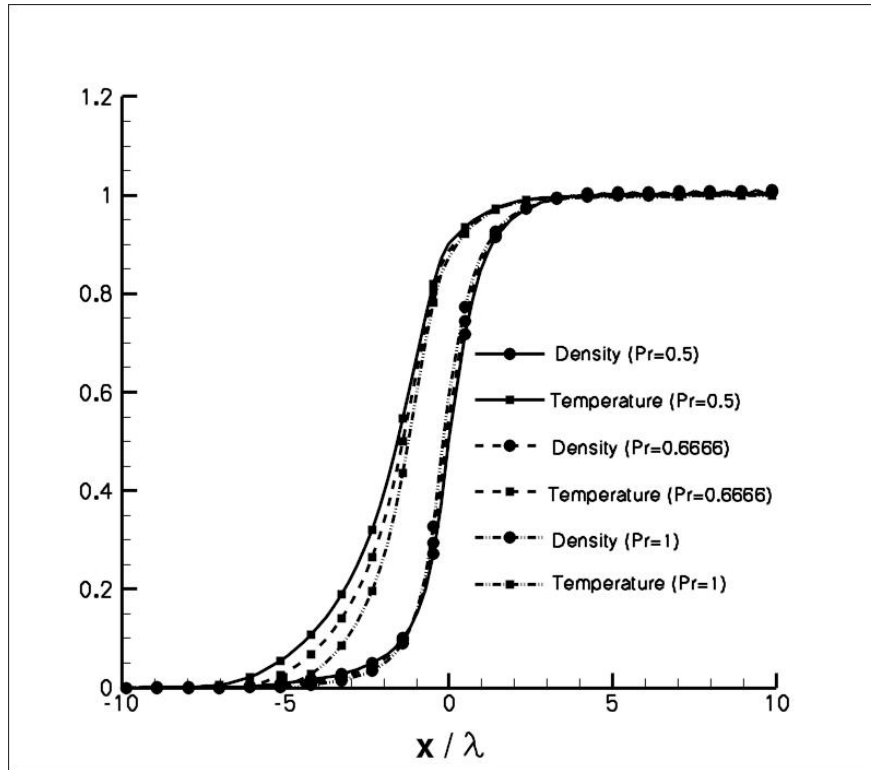


Figure 22. Accuracy of gas kinetic scheme: Effect of varying Prandtl number in Mach 5 shock wave with hard sphere collision model

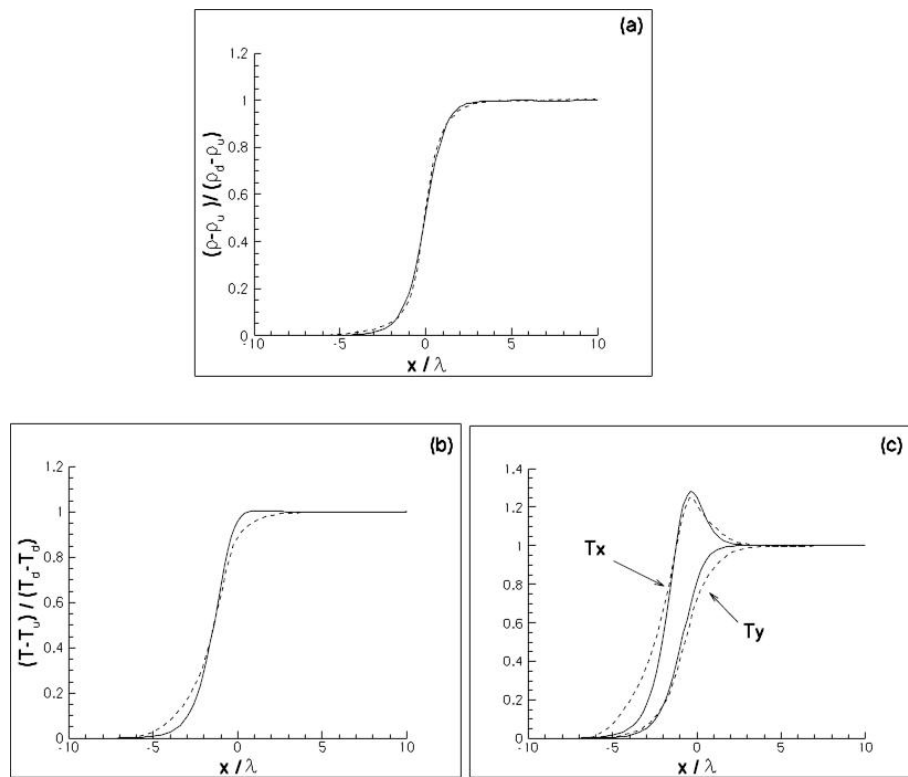


Figure 23. Accuracy of gas kinetic scheme: Macroscopic parameters inside a Mach 5 shock wave with hard sphere collision model, a) density, (b) temperature, (c) Streamwise and normal components of temperature.
 - - - - - Gas Kinetic Scheme
 _____ Boltzmann (Present)